

# **1 Origin of deep ocean microseisms by using teleseismic 2 body waves**

Matthieu Landès,<sup>1</sup> Fabien Hubans,<sup>2</sup> Nikolai M. Shapiro,<sup>1</sup> Anne Paul,<sup>2</sup> and  
Michel Campillo,<sup>2</sup>

---

M. Landès, Équipe de sismologie, Institut de Physique du Globe de Paris, 4 place Jussieu,  
75252, PARIS, France. (landes@ipgp.jussieu.fr)

F. Hubans, Laboratoire de Géophysique Interne et Tectonophysique , Maison des géosciences,  
BP 53, 38041 GRENOBLE CEDEX 9, France. (fabien.hubans@obs.ujf-grenoble.fr)

N. M. Shapiro, Équipe de sismologie, Institut de Physique du Globe de Paris, 4, place Jussieu,  
75252, PARIS, France. (nshapiro@ipgp.jussieu.fr)

A. Paul, Laboratoire de Géophysique Interne et Tectonophysique , Maison des géosciences, BP  
53, 38041 GRENOBLE CEDEX 9, France. (Anne.Paul@obs.ujf-grenoble.fr)

M. Campillo, Laboratoire de Géophysique Interne et Tectonophysique , Maison des géosciences,  
BP 53, 38041 GRENOBLE CEDEX 9, France. (Michel.Campillo@ujf-grenoble.fr )

<sup>1</sup>IPGP, CNRS, France

<sup>2</sup>LGIT, Université Joseph Fourier, CNRS,

France

**Abstract.**

Recent studies of oceanic microseisms have concentrate on fundamental-mode surface waves. Extraction of fundamental-mode Rayleigh and Love wave Green functions from station-station correlations of ambient seismic noise has recently been demonstrated to be a very powerful tool for imaging of the Earth's crust and uppermost mantle.

In this study we concentrate on energetic arrivals in two frequency bands around the primary (14s) and the secondary (7s) microseismic peaks that appear at near-zero times in noise cross-correlations. Thanks to a polarisation analysis of data from the the ETSE network (Turkey), we identify this "near-zero time" signal as an upcoming P wave in the secondary microseismic frequency band (5-10s). In a second step, analysing noise cross-correlations from three different arrays ( in Yellowstone, in Turkey and in Kyrgyzstan), we determine the origin of these signals by means of beamforming analysis and its projection on the Earth.

Our results show that, in the 0.1-0.3 Hz frequency band, the energetic "near-zero" time arrivals in seismic noise cross-correlations are mainly formed by teleseismic P, PP, and PKP waves. Generation of this ambient body waves in the secondary microseismic band presents a marked seasonal behaviour with sources located in southern and northern oceans during summer and winter, respectively. Moreover, body wave array analysis is accurate enough to confirm that significant amount of the microseism energy is generated far from the coast in deep oceans.

## 1. Introduction

26 Recent years witnessed a strong interest in studying background seismic noise. One  
27 of the reasons for this interest is the possibility to extract deterministic Green functions  
28 from correlations of a random wavefield that can be proved mathematically with different  
29 approaches (e.g., *Lobkis and Weaver* [2001]; *Snieder* [2004]; *Gouédard et al.* [2008]) and  
30 that has been demonstrated in acoustic laboratory experiments (e.g., *Lobkis and Weaver*  
31 [2001]; *Derode et al.* [2003]). Application of this principle to large amount of continuous  
32 digital seismic records provided by modern networks provides us with new approaches for  
33 seismic tomography (e.g., *Shapiro and Campillo* [2004]; *Shapiro et al.* [2005]; *Sabra et al.*  
34 [2005]; *Yang et al.* [2007]; *Stehly et al.* [2009]) and monitoring (e.g., *Sens-Schönfelder and*  
35 *Wegler* [2006]; *Brenguier et al.* [2008b]; *Brenguier et al.* [2008a]). Detailed analysis of  
36 high-quality continuous records also allows us to better understand the origin of the am-  
37 bient seismic noise and its relation to oceanic and atmospheric processes. New methods of  
38 noise-based seismic imaging and monitoring are based on a principle that the Green func-  
39 tion between two points can be extracted by correlating a random wavefield recorded by  
40 receivers located in these points. In other words, one of the two receivers can be considered  
41 as a virtual source recorded by the second receiver. This principle is especially attractive  
42 when applied in context of random wavefield recorded by a network of numerous recorders.  
43 In this case, by computing all possible inter-station cross-correlations it becomes possible  
44 to place virtual sources at every receiver location and to have their records by the whole  
45 network resulting in a very dense path coverage. The deterministic waveforms (Green  
46 functions) extracted from the cross-correlations can be used then to measure and to in-

47 vert travel times with different methods developed in context of earthquake or explosion  
48 based seismology.

49 The noise based Green function reconstruction implies, however, some strong hypothe-  
50 sis about the noise modal composition. A perfect reconstruction can be achieved for an  
51 ideally random and equipartitioned wavefield (*Lobkis and Weaver* [2001]; *Sánchez-Sesma*  
52 *and Campillo* [2006]). In a case of seismic noise it would imply that its sources should be  
53 distributed randomly and homogeneously in volume. This is obviously not the case for  
54 the real ambient seismic noise within the Earth. First, most of its sources are located on  
55 the surface resulting in stronger presence of fundamental mode surface waves and their  
56 relatively easy reconstruction from inter-station cross-correlations. For the same reasons,  
57 extracting body wave Green functions from noise cross-correlations remains challenging.  
58 Second, the distribution of noise sources is not perfectly random and homogeneous. Back-  
59 ground seismic oscillations are mostly generated by the forcing from oceanic gravity and  
60 infragravity waves. The interaction between these oceanic waves and the solid Earth is  
61 governed by a complex non-linear mechanism (e.g., *Longuet-Higgins* [1950]) and, as a  
62 result, the noise excitation depends on many factors such as the intensity of the oceanic  
63 waves but also the intensity of their interferences as well as the seafloor topography (e.g.,  
64 *Kedar et al.* [2008]). Overall, the generation of seismic noise is strongly modulated by  
65 strong oceanic storms and therefore, has a clear seasonal and non-random pattern.

66 Distribution of noise sources homogenizes when considered over long times (more than  
67 one year). The homogenization and randomization of the noise wavefield is also enhanced  
68 by the scattering of the seismic waves on the small-scale heterogeneity within the Earth.  
69 Also, because of the stationary phase principle, a cross-correlation of the noise recorded

70 by two receivers is dominated by contribution from sources located in vicinity of the line  
71 connecting these receivers. Therefore, even without a perfectly homogeneous distribu-  
72 tion, a presence of sufficient amount of favorably located noise sources results in relatively  
73 high quality reconstruction of fundamental mode surface waves. As a consequence, recon-  
74 structing surface waves from correlations of seismic noise and measuring their dispersion  
75 curves works rather well. However, further improving the accuracy of the noise based  
76 measurements needed to develop new high-resolution imaging and monitoring methods  
77 requires better understanding of the noise modal content and its evolution in space and  
78 time. Taking into account realistic distribution of noise sources is also necessary to be  
79 able to apply waveform inversion approaches to the noise correlations.

80 Seismic noise spectra contains two prominent peaks at 0.05 - 0.1 and 0.1 - 0.3 Hz called  
81 primary and secondary microseisms, respectively. The primary microseism originates from  
82 direct forcing of strong oceanic waves while the secondary microseism which is character-  
83 ized by stronger amplitudes is produced at double frequency by a non-linear interaction  
84 of these waves as suggested by *Longuet-Higgins* [1950]. Both microseismic peaks are dom-  
85 inated by fundamental mode surface waves. It is currently debated whether the surface  
86 wave component of microseisms is generated primarily along coastlines (e.g., *Friedrich*  
87 *et al.* [1998]; *Bromirski and Duennebier* [2002]; *Essen et al.* [2003]; *Schulte-Pelkum et al.*  
88 [2004]; *Rhie and Romanowicz* [2006]; *Yang and Ritzwoller* [2008]) or if it is also generated  
89 in deep-sea areas (*Cessaro* [1994]; *Stehly et al.* [2006]; *Chevrot et al.* [2007]; *Kedar et al.*  
90 [2008]). At the same time, body waves were detected in the secondary microseismic band  
91 using dense seismic arrays (e.g., *Backus et al.* [1964]; *Toksöz and Lacoss* [1968]; *Seriff et al.*  
92 [1965]; *Iyer and Healy* [1972]; *Koper and de Foy* [2008]; *Gerstoft et al.* [2008]) and can

93 be often associated with specific storms (e.g., *Gerstoft et al.* [2006]). Inhomogeneous dis-  
94 tribution of noise sources is clearly revealed by the asymmetry of noise cross-correlations  
95 observed in both primary and secondary microseismic bands (e.g., *Stehly et al.* [2006];  
96 *Yang and Ritzwoller* [2008]). According to Longuet-Higgins' theory, the generation of  
97 secondary microseisms is associated with the non-linear interaction of swells propagating  
98 in opposite directions. Such a configuration can be encountered in the coastal region  
99 where incident and reflected waves are likely present. This is the case that is considered  
100 as prominent by the seismologists based on the observations of the radiation by individual  
101 storms (e.g., *Bromirski and Duennebier* [2002]; *Gerstoft and Tanimoto* [2007]; *Bromirski*  
102 [2009]). Although there is little doubt that a part of the ambient noise is related with  
103 the interaction of oceanic waves with the coast, it is not the only situation where waves  
104 propagating in opposite directions are encountered. *Kedar et al.* [2008] used a wave action  
105 model to implement Longuet Higgins theory and found that particular regions in the deep  
106 oceans are potential sources of secondary microseism excitation. This is related to spe-  
107 cific conditions of meteorological forcing associated with resonances of the water column.  
108 Their results indicate that secondary microseisms can be generated in specific deep-water  
109 areas with one example in the Atlantic ocean south of Greenland.

110 To investigate the location of the sources of the background noise, we use seismological  
111 data averaged over long time series. The Rayleigh wave part of the noise in the secondary  
112 microseism period band rapidly attenuates with distance. It is therefore difficult to assess  
113 the locations of sources when the signal is dominated by the closest source, often the  
114 closest coast, that hides the remote sources. To overcome this difficulty, we use P wave  
115 at teleseismic distances recorded in continental environments.

116 We compute noise cross-correlations for three seismic arrays located within continents  
117 in the Northern hemisphere. During summer months, when most of strong storms are  
118 located in the Southern hemisphere, the observed noise cross-correlations are dominated  
119 by arrivals at near-zero times. Polarization analysis clearly indicates that these arrivals  
120 are composed of teleseismic P-waves. We then use a beamforming analysis to determine  
121 precisely back-azimuths and slowness corresponding to these arrivals and to backproject  
122 them to the regions where the energy was generated based on ray-tracing in a global  
123 spherically symmetric Earth model.

### 1.1. Polarization analysis to detect teleseismic P-waves in noise cross-correlations

124 In this section, we use the data of the Eastern Turkey Seismic Experiment (ETSE) that  
125 operated a temporary network of 20 broadband stations between October 1999 and August  
126 2001 (Figure 1) (*Sandvol et al.* [2003]).

#### 1.1.1. Data pre-processing

128 Polarization analysis of noise cross-correlations requires preserving the amplitude ratio  
129 between components. Therefore, standard processing for the computation of noise cross-  
130 correlations such as one-bit normalization and spectral whitening, can not be applied.  
131 Instead, data are corrected for instrumental responses, resampled to 1 Hz and filtered  
132 between 0.01 and 0.3 Hz. A water level of 4 times the standard deviation of each record is  
133 used to decrease the amplitude effect of earthquakes on cross-correlations. Furthermore,  
134 for each station and each component, only daily records with mean energy smaller than  
135 the whole experiment mean energy are used for the polarization analysis.

#### 1.1.2. Noise cross-correlations

137 Figures 2 and 3 show cross-correlations between vertical noise records (ZZ) plotted with  
138 respect to distance between stations for two different seasons and two frequency bands  
139 which correspond to primary and secondary microseismic peaks (0.05-0.1 Hz and 0.1-0.3  
140 Hz). A propagating wave with apparent velocity close to 3 km/s (red dashed lines) is  
141 observed at negative and positive times. This time-symmetrical signal which is stronger  
142 in the 0.05-0.1 Hz bandpass (Figures 2a and 3a) is the Rayleigh wave part of the Green  
143 function reconstructed from random noise correlations. Another signal with apparent ve-  
144 locity larger than 10 km/s (blue dashed lines) is dominant in the 0.1-0.3 Hz bandpass  
145 (Figures 2a and 3a). This signal with very high apparent velocity is stronger during  
146 northern summer than winter. We hypothesize that those fast arrivals are P waves with  
147 steep incidence angle that are generated by very distant sources. During northern summer  
148 strong secondary microseisms are mostly expected to be generated within oceans in the  
149 southern hemisphere. For such sources, relatively short period surface-waves are attenu-  
150 ated because of large propagating distances. This may explain why the noise correlations  
151 are dominated by near-zero-time body wave arrivals. We test this hypothesis with a po-  
152 larization analysis on cross-correlation signals. We demonstrate that the polarization of a  
153 plane wave recorded at two stations can be reliably estimated from the multicomponent  
154 cross-correlations.

### 155 **1.1.3. Polarization analysis of a plane wave from its cross-correlation records** 156 **: Method**

157 *Jurkevics* [1988] studied the polarization of different waves emitted by an earthquake using  
158 the covariance matrix of 3-component record. He recovered the polarization angle and the  
159 azimuth from the eigenvectors of the covariance matrix. We demonstrate in the Appendix



160 that the covariance matrix of the components at a single station ( $S_{CovSig}$ ) is proportional  
 161 to the covariance matrix of the cross-correlation signals ( $S_{CovCorr}$ ) (Equation A10) for  
 162 a plane P-wave propagating across a network of stations. Therefore, the eigenvectors  
 163 are identical and the polarization analysis can be performed either on cross-correlations  
 164 records at 2 stations or on 3-component record at a single station.

165 As suggested by *Jurkevics* [1988], the eigenvalues of the covariance matrix ( $\lambda_1 > \lambda_2 >$   
 166  $\lambda_3$ ) are used to compute the coefficient of rectilinearity  $R$ :

$$R = 1 - \frac{\lambda_2 + \lambda_3}{2\lambda_1}. \quad (1)$$

167 which is equal to 1 for a rectilinear polarization. The eigenvector corresponding to the  
 168 largest eigenvalue  $\lambda_1$  gives the polarization angle and azimuth of the plane wave. The  
 169 conversion from the polarization angle ( $\varphi$ ) to the incidence angle ( $I$ ) is obtained from  
 170 the displacement equations for a reflected P wave at the free surface given by *Aki and*  
 171 *Richards* [1980].

172 We use a ratio between P and S waves velocities of :  $V_P/V_S = \sqrt{3}$  for this conversion.

#### 173 **1.1.4. Polarization analysis of cross-correlations computed with ETSE data**

174 We use only station pairs with distance larger than 50 km to compute the covariance  
 175 matrix of the 3 cross-correlations ZE, ZN and ZZ. To prevent any influence of the Rayleigh  
 176 wave (group velocity 3 km/s), we select time windows between -10s and 10s. Among the  
 177 127,490 cross-correlation signals available for 671 days and 190 station pairs, 23,449 signals  
 178 are selected based on signal-to-noise (see section 1.1.1) and minimum distance criterion.  
 179 This rather small percentage (18%) is due to time-variable data availability and quality.

180 Daily records including earthquakes or glitches are removed from the database due to our  
181 water-level amplitude filter.

182 Using eigenvalues and eigenvectors of the covariance matrix, we compute the rectilin-  
183 earity coefficient (equation 1), the azimuth and the incidence angle for every inter-station  
184 cross-correlation. The rectilinearity coefficient over the whole experiment is  $0.84 \pm 0.12$ ,  
185 which shows that the polarization of the studied wave is almost linear.

186 Figure 4 shows particle motion for 2 daily cross-correlations and 2 station pairs. Particle  
187 motion is shown in the horizontal plane (ZN as a function of ZE) and in the vertical  
188 propagation plane defined by the measured azimuth angle (ZZ as a function of ZH) where  
189 ZH is obtained by the rotation of the ZE and ZN components of the correlations using the  
190 azimuth angle measured from the polarization analysis. The rotation can be computed  
191 after the correlation because no non-linear processing such as one-bit transform or spectral  
192 whitening has been applied to the data. The red dashed lines in Figure 4 display the  
193 azimuth and incidence angle obtained from the covariance method. We observe that the  
194 displacement is stronger on the vertical component than on the horizontal ones suggesting  
195 that the signal observed on the cross-correlations at near-zero times is composed of nearly  
196 vertically incident P waves.

197 We then estimate the incidence angle and the azimuth of the body wave detected from  
198 correlations of ambient noise records and investigate their possible seasonal variations.  
199 Figure 5 shows the probability of occurrence of a given value of incidence angle (Figure  
200 5a) and azimuth (Figure 5b) in a time period of 20 days evaluated from all daily records  
201 and station pairs. Figure 5a shows that we detect P waves with steep incidence angles  
202 during the whole experiment. It also documents a seasonal change of the incidence angle

203 from an average of  $15^\circ$  in summer to  $25^\circ$  in winter, with a more accurate measurement of  
204 the incidence angle in the summer than in the winter (larger probability of occurrence).  
205 We observe the exact opposite in Figure 5b with better determined azimuths in winter  
206 than in summer, simply because the azimuth can not be evaluated for an almost vertically  
207 incident P wave.

208 The seasonal variation observed for the incidence angle is even clearer for the azimuth  
209 (Figure 5b). In summer, the average azimuth close to  $0^\circ$  shows that sources of the P waves  
210 are located south of the ETSE network. Winter noise sources are located north-west of  
211 the network as documented by azimuths close to  $150^\circ$ . Those observations are consistent  
212 with seasonal changes in the behavior of seismic noise sources (e.g. *Stehly et al.* [2006];  
213 *Tanimoto et al.* [2006]). The precise location of the sources of the P wave component of  
214 the noise will be investigated in the following section.

## 2. Locating seismic noise sources with a beamforming analysis

215 To determine regions that generate these body waves, we perform a beamforming anal-  
216 ysis of the noise cross-correlations using the whole network as an array. We use only  
217 vertical components where the body waves are mostly detected. When studying a single  
218 component, we do not need to preserve the amplitude and, for efficiency, pre-process the  
219 continuous data with spectral whitening and one-bit normalization to improve the signal-  
220 to-noise ratio (*Larosse et al.* [2004]). We analyze two frequency bands [0.05-0.1Hz] and  
221 [0.1-0.3Hz] corresponding to primary and secondary microseismic peaks, respectively.

## 2.1. Beamforming analysis

Our time-shift beamforming analysis consists of decomposing the body-wave part of a wavefield recorded by a network into plane waves. If a plane wave defined by its slowness vector  $\vec{S}$  reaches two stations A and B, the cross-correlation of signals recorded at these stations will be shifted by:

$$\Delta T_{AB}(\vec{S}) = \vec{S} \cdot \vec{AB} \quad (2)$$

where  $\vec{AB}$  is the vector connecting A and B. We approximate the network to be flat by neglecting different station elevations and project the slowness vectors into the horizontal plane considering its South-North and West-East components  $S_N$  and  $S_E$ . For a given horizontal slowness vector  $\vec{S} = (S_E, S_N)$ , we time-shift all inter-station cross correlations following (2) and stack them to define the function  $C_{\text{stack}}$  :

$$C_{\text{stack}}(\vec{S}, t) = iFFT \left( \sum_{P \in PS} e^{2i\pi\omega \Delta T_P(\vec{S})} C_P(\omega) \right) \quad (3)$$

where  $PS$  represents the ensemble of pairs of stations,  $C_P$  is the Fourier Transform of the noise correlation for pair  $P$  and  $iFFT$  is the inverse Fourier transform. The characterization of the signal amplitude in the horizontal slowness domain is finally defined as :

$$A(\vec{S}) = \int_{-T}^T \Gamma \left( C_{\text{stack}}(\vec{S}, t) \right) dt \quad (4)$$

222 where  $\Gamma[f(t)]$  returns the envelope of the function  $f(t)$  using Hilbert transform. Integra-  
 223 tion limits  $[-T, T]$  are used to select the part of cross-correlations centered at targeted  
 224 slowness and we set  $T$  to be equal 15s and 10s for the primary and the secondary micro-  
 225 seismic bands, respectively.

226 Figure 6a shows results of the beamforming analysis applied to one-month cross-  
227 correlations of the noise recorded by the ETSE network during August 2000 and filtered  
228 around the secondary microseismic peak (0.1-0.3 Hz). Energy distribution on the hori-  
229 zontal slowness plane is clearly not random and homogeneous. Two clear patches indicate  
230 that during this month most of body-wave energy recorded by ETSE stations is arriving  
231 with rather fast apparent velocities ( $> 20$  km/s) and is coming from two preferential di-  
232 rections south and south-east of the network. A similar analysis made during February  
233 2001 also shows two very localized patches of body wave energy with fast apparent ve-  
234 locities ( Figure 6b). However, during this winter month the waves are coming from the  
235 north. These observation are in good agreement with seasonal variations of the location of  
236 sources of microseisms deduced from the polarization analysis and from previous studies  
237 (e.g. *Stehly et al.* [2006]).

238 We then analyzed seismic noise recorded by a network operated in 2000-2001 in North  
239 America, i.e., by the Yellowstone PASSCAL experiment (*Fee and Dueker* [2004]). Results  
240 of the beamforming analysis for August 2000 and February 2001 shown in Figures 6c and  
241 6d, respectively, are similar to observations made with the ETSE network. Localized noise  
242 sources are seen south of the network during the Northern hemisphere summer and north  
243 of the network during the winter.

## 2.2. Locating P-wave noise sources on the Earth's surface.

244 In a next step, we project the results of the beamforming analysis on the Earth's surface.  
245 Following the results of the polarization analysis of the near-zero-time arrivals at cross-  
246 correlations and their fast apparent velocities, we assume that they are mostly composed  
247 of teleseismic P-waves. For a given slowness and back-azimuth we can back-project a

248 seismic wave using a ray tracing in a spherically symmetric Earth's model. We suppose  
249 that diffracted and reflected phases are less energetic than direct and refracted waves and,  
250 therefore, the waves that we take into account are P, PP, PKP, PKiKP and PKIKP waves  
251 and we use the IASPEI91 tables (*Kennett and Engdahl* [1991]) to relate the slowness with  
252 the source-receiver distance for all considered phases (Figure 7).

253 For every point on the Earth's surface, we identify all phases that may propagate from  
254 this point to the network location and determine their horizontal slowness. Therefore,  
255 for each position we determine the "energy" of all the waves that are considered from  
256 the horizontal slowness plane. The energy is evaluated from the function  $A$  determined  
257 by the beamforming analysis (equation 4). Finally, we select the phase corresponding  
258 to the maximum value of the beamforming map and attribute this amplitude to the  
259 projection at the considered geographical position. By repeating this procedure for all  
260 points on a  $5^\circ$  longitude  $\times$   $2.5^\circ$  latitude geographical grid we construct a map of what can  
261 be considered as probability density of noise sources during the considered period.

262 This process is illustrated for three geographical locations shown with stars in Figure  
263 8b and ETSE Network (triangle in Figure 8b). White lines are the great circles and their  
264 projections in the horizontal slowness plane in Figure 8b and 8a. For the location 1, the  
265 possible seismic phases are PP, PKP (branches **ab** and **bc**) and PKiKP (red line in 8a)  
266 and the branch **bc** of the phase PKP corresponds to the strongest amplitude that is then  
267 selected for the projections. Similarly, for locations 2 and 3, possible phases are PKiKP  
268 and P or PP, respectively, and the latter correspond to stronger amplitudes and are used  
269 for the projection. The larger patch is projected as a P wave into the Indian ocean and

270 as a PP wave into the southern Pacific. The smaller patch corresponds to a PKP wave  
271 originated in the vicinity of New Zealand.

272 Maps of P-wave noise source densities corresponding to beamfoming results from Fig-  
273 ure 6 are shown in Figure 9. Some source areas such as the region south of Africa during  
274 August 2000 and Northern Atlantic south of Iceland during February 2001 are well illu-  
275 minated by both networks. This suggests that strongest sources of P-waves microseisms  
276 are seen by multiple networks distributed around the world. Therefore, we decided to  
277 combine observations from different networks to improve the accuracy of the location of  
278 main sources of P-wave microseisms. We used stations from three networks shown in Fig-  
279 ure 1: 46 stations from Yellowstone park, 29 stations from ETSE, and 14 stations of the  
280 Kirgыз Seismic Network (KNET). We interpret the projection map obtained from every  
281 individual networks as a probability density and just multiply them to find the combined  
282 distribution.

283 Location of P-wave sources of the primary and secondary microseisms during different  
284 seasons are shown in Figures 10 and 11. For every map we used correlations of one month  
285 of data. In the secondary microseismic band, regions that generate P-waves are well de-  
286 fined (Figure 10) and are mostly in deep oceans. Also, a clear seasonal migration can be  
287 observed with strongest sources located in the northern hemisphere during the northern  
288 hemisphere winter and in the southern hemisphere during the summer. In the primary  
289 microseismic band (Figure 11) we also observe a similar seasonal variation. However,  
290 uncertainties of the source location are much larger than in the secondary microseismic  
291 band. The reason for this is that the signal-noise ratio of the near-zero-time arrival in  
292 cross-correlations is much lower in the primary microseismic band than in the secondary

293 microseismic band. Also, reliability of the array analysis degrades at longer wavelengths.  
294 Despite these large uncertainties, it is clearly seen in Figures 10 and 11 that, in most  
295 cases, sources of primary microseisms do not coincide geographically with sources of sec-  
296 ondary microseisms pointing to different physical mechanism of generation of these two  
297 microseismic peaks.

298 The maps of Figure 11 are similar with the results of *Stehly et al.* [2006] in terms of  
299 seasonality. The location of noise sources based on the backpropagation of Rayleigh  
300 waves can not provide a resolution comparable to the one we achieved with body waves.  
301 Nevertheless, even with P waves, the uncertainties of location of sources of the primary  
302 microseism do not allow to clearly conclude unambiguously that they are located in deep  
303 parts of the ocean, in near-coastal regions, or both. While strongest identified source  
304 areas tend to extend to deep oceanic parts, they also cover coastal areas.

### 3. Discussion and conclusion

305 Results of our polarization and beamforming analyses of the continuous noise records  
306 demonstrate that significant part of the microseismic noise is composed of P-waves gen-  
307 erated by distant sources. These sources show a clear seasonality in correlation with the  
308 seasonal migration of the strong oceanic storms between the southern and the northern  
309 hemisphere suggesting that the observed teleseismic P-waves are generated by the inter-  
310 action of waves produced by these storms with the seafloor. Location of P-wave sources  
311 in the primary and in the secondary microseismic bands do not coincide with each other  
312 indicating that these two peaks are generated in different regions and possibly by different  
313 physical process. P-waves are more easily identified in the secondary microseismic band  
314 than in the primary microseismic band. While we cannot exclude that this difference is



315 related to the more efficient mechanism generating secondary microseismic P-waves than  
316 primary ones, a simple explanation of this observation can be related to difference in wave  
317 propagation. Strong noise sources generate both body wave and surface waves. For the  
318 latter, their attenuation is much stronger at higher frequencies. Therefore, surface waves  
319 in the secondary microseismic peak propagate much less efficiently over very long distances  
320 than in the low-frequency primary microseismic band. As a consequence, for distant noise  
321 sources, the relative part of the body waves in the recorded seismic noise is relatively high  
322 in the secondary microseismic band while the primary microseismic band remains largely  
323 dominated by surface waves, making observation of P-waves more difficult.

324 Using array-based processing of the teleseismic P-waves to locate regions generating  
325 strong microseisms has significant advantages relative to using surface waves (e.g., *Stehly*  
326 *et al.* [2006]). The latter yields only a determination of their back-azimuths at the  
327 array location while with body waves we can measure both backazimuths and slownesses  
328 that can be converted into distances. Therefore, we can locate the source regions more  
329 accurately with body waves than with surface waves.

330 We can compare our maps of the source density in the secondary microseismic band  
331 (Figure 10) with results by *Gerstoft et al.* [2008] who applied beamforming to the noise  
332 records of the Southern California seismic network. We find similar source locations in  
333 southern Pacific and Indian oceans during summer months and in northern Pacific and  
334 Atlantic ocean during winter months. Using three networks simultaneously allows us to  
335 image source regions with higher reliability. One of most important consequences of this  
336 improved reliability is that we clearly see that strongest sources of P-wave microseisms are  
337 located in deep oceans far from coasts for the secondary microseism. Also, the observed

338 source regions are significantly smaller than areas affected by significant wave heights.  
339 Overall our observations are consistent with the generation of microseisms by non-linear  
340 interaction of ocean waves propagating in opposite directions that create a pressure dis-  
341 tribution on the seafloor at twice the frequency of the interfering waves (*Longuet-Higgins*  
342 [1950]). Following *Kedar et al.* [2008], this wave-wave interaction occurs in deep oceans  
343 and the geographical intensity of this interaction may be computed from oceanic wave ac-  
344 tion models. Moreover, the efficiency of the coupling between the interfering oceanic waves  
345 and the seafloor may depend on the depth of the water column, i.e., on the bathymetry.  
346 As a result, an efficient transfer of energy from oceanic to seismic waves occurs over geo-  
347 graphically very limited and specific areas. It is in particular interesting to note that the  
348 source area near Iceland seen in Figure 10 during October and January coincides with  
349 the strong source of Rayleigh wave microseisms computed by *Kedar et al.* [2008] based on  
350 Longuet-Higgins's theory and oceanic wave action models.

351 These observations confirm that the source of secondary microseisms are not confined  
352 in the coastal areas as it is often accepted by seismologists. On average, the excitation of  
353 P waves by oceanic waves is stronger in the deep oceans. It does not mean, however, that  
354 there is no excitation along the coast, particularly when storms hit the shoreline.

355 In the future, locating sources of P-wave microseisms can be improved with using more  
356 networks better distributed over the globe. Observing and understanding these sources is  
357 important to validate predictive models of the seismic noise generation and distribution.  
358 These models, in turn, may help us to improve the accuracy of noise based seismic imaging  
359 and monitoring.

360 **Acknowledgments.** The data of the "Eastern Turkey" and of the "Geodynamics of  
361 the Yellowstone Hotspot" seismic PASSCAL experiment as well as of the Kyrgyz Seismic  
362 Network used in this study were obtained through IRIS DMC. We thank Sharon Kedar  
363 and Frank Webb for helpful discussions and G. Moguilny for maintaining the Cohersis  
364 cluster. This work was supported by Agence Nationale de la Recherche (France) under  
365 contract ANR-06-CEXC-005 (COHERSIS) and by a EU project WHISPER.

## References

- 366 Aki, K., and P. Richards, *Quantitative seismology-Theory and Methods*, W. H. Freeman,  
367 1980.
- 368 Backus, M., J. Burg, D. Baldwin, and E. Bryan, Wide-band extraction of mantle p waves  
369 from ambient noise, *Geophysics*, *39*, 672–692, 1964.
- 370 Brenguier, F., M. Campillo, C. Hadziioannou, N. M. Shapiro, R. M. Nadeau, and L. E.,  
371 Postseismic Relaxation Along the San Andreas Fault at Parkfield from Continuous  
372 Seismological Observations, *Science*, *321*, 1478, doi:10.1126/science.1160943, 2008a.
- 373 Brenguier, F., N. Shapiro, M. Campillo, V. Ferrazzini, Z. Duputel, O. Coutant, and  
374 A. Nercessian, Towards forecasting volcanic eruptions using seismic noise, *Nature*,  
375 doi:10.1.1038/ngeo104, 2008b.
- 376 Bromirski, P., Earth vibrations, *Science*, *324*(5930), 1026, 2009.
- 377 Bromirski, P., and F. Duennebier, The near-coastal microseism spectrum: Spatial and  
378 temporal wave climate relationships, *J. Geophys. Res.*, *107*, 2166, 2002.
- 379 Cessaro, R. K., Sources of primary and secondary microseisms, *Bull. Seismol. Soc. Am.*,  
380 *84*, 142–148, 1994.

- 381 Chevrot, S., M. Sylvander, S. Benahmed, C. Ponsolles, J. M. Lefèvre, and D. Paradis,  
382 Source locations of secondary microseisms in western Europe: Evidence for both coastal  
383 and pelagic sources, *Journal of Geophysical Research (Solid Earth)*, *112*(B11), 11,301–  
384 +, doi:10.1029/2007JB005059, 2007.
- 385 Derode, A., E. Larose, M. Tanter, J. de Rosny, A. Tourin, M. Campillo, and M. Fink, Re-  
386 covering the Green's function from field-field correlations in an open scattering medium  
387 (L), *Acoustical Society of America Journal*, *113*, 2973–2976, doi:10.1121/1.1570436,  
388 2003.
- 389 Essen, H.-H., F. Krüger, T. Dahm, and I. Grevemeyer, On the generation of secondary  
390 microseisms observed in northern and central Europe, *Journal of Geophysical Research*  
391 (*Solid Earth*), *108*, 2506–+, doi:10.1029/2002JB002338, 2003.
- 392 Fee, D., and K. Dueker, Mantle transition zone topography and structure beneath the Yel-  
393 lowstone hotspot, *Geophysical Research Letters*, *31*, 18,603, doi:10.1029/2004GL020636,  
394 2004.
- 395 Friedrich, A., F. Krüger, and K. Klinge, Ocean-generated microseismic noise located with  
396 the Gräfenberg array, *Journal of Seismology*, *2*, 47–64, doi:10.1023/A:1009788904007,  
397 1998.
- 398 Gerstoft, P., and T. Tanimoto, A year of microseisms in southern California, *Geophysical*  
399 *Research Letters*, *34*, 20,304–+, doi:10.1029/2007GL031091, 2007.
- 400 Gerstoft, P., M. C. Fehler, and K. G. Sabra, When Katrina hit California, *Geophysical*  
401 *Research Letters*, *33*, 17,308, doi:10.1029/2006GL027270, 2006.
- 402 Gerstoft, P., P. M. Shearer, N. Harmon, and J. Zhang, Global P, PP, and PKP wave  
403 microseisms observed from distant storms, *Geophysical Research Letters*, *35*, 23,306,

- 404 doi:10.1029/2008GL036111, 2008.
- 405 Gouédard, P., L. Stehly, F. Brenguier, M. Campillo, Y. Colin de Verdière, E. Larose,  
406 L. Margerin, P. Roux, F. J. Sánchez-Sesma, N. M. Shapiro, and R. L. Weaver, Cross-  
407 correlation of random fields: mathematical approach and applications, *Geophysical*  
408 *Prospecting*, *56*, 2008.
- 409 Iyer, H. M., and J. H. Healy, evidence for the existence of locally-generated body waves in  
410 the short-period noise at the large aperture seismic array, *Bull. Seismol. Soc. Am.*, *62*,  
411 13–29, 1972.
- 412 Jurkevics, A., Polarization analysis of three-component array data, *Bull. Seism. Soc. Am.*,  
413 *78*(5), 1725–1743, 1988.
- 414 Kedar, S., M. Longuet-Higgins, F. Webb, N. Graham, R. Clayton, and C. Jones, The  
415 origin of deep ocean microseisms in the North Atlantic Ocean, *Royal Society of London*  
416 *Proceedings Series A*, *464*, 777–793, doi:10.1098/rspa.2007.0277, 2008.
- 417 Kennett, B. L. N., and E. R. Engdahl, Traveltimes for Global Earthquake Loca-  
418 tion and Phase Identification, *Geophysical Journal International*, *105*, 429–465, doi:  
419 10.1111/j.1365-246X.1991.tb06724.x, 1991.
- 420 Koper, K. D., and B. de Foy, Seasonal Anisotropy in Short-Period Seismic Noise Recorded  
421 in South Asia, *Bull. Seism. Soc. Am.*, *98*(6), 3033–3045, doi:10.1785/0120080082, 2008.
- 422 Larosse, E., A. Derode, M. Campillo, and M. Fink, Imaging from one-bit correlations of  
423 wideband diffuse fields, *Appl. Phys. Lett.*, *95*, 8393–8399, 2004.
- 424 Lobkis, O. I., and R. L. Weaver, On the emergence of the green’s function in the corre-  
425 lations of a diffuse field, *Journal of Acoustic Society of America*, *110*(6), 3011–3017,  
426 2001.

- 427 Longuet-Higgins, M. S., A Theory of the Origin of Microseisms, *Royal Society of London*  
428 *Philosophical Transactions Series A*, 243, 1–35, 1950.
- 429 Rhie, J., and B. Romanowicz, A study of the relation between ocean storms  
430 and the Earth’s hum, *Geochemistry, Geophysics, Geosystems*, 7, 10,004–+, doi:  
431 10.1029/2006GC001274, 2006.
- 432 Sabra, K., P. Gerstoft, P. Roux, W. Kuperman, and M. Fehler, Surface wave tomogra-  
433 phy from seismic ambient noise in Southern California, *Acoustical Society of America*  
434 *Journal*, 117, 2431–2432, 2005.
- 435 Sánchez-Sesma, F. J., and M. Campillo, Retrieval of the Green’s Function from Cross  
436 Correlation: The Canonical Elastic Problem, *Bull. Seism. Soc. Am.*, 96(3), 1182–1191,  
437 doi:10.1785/0120050181, 2006.
- 438 Sandvol, E., N. Turkelli, E. Zor, R. Gok, T. Bekler, C. Gurbuz, D. Seber, and  
439 M. Barazangi, Shear wave splitting in a young continent-continent collision: An ex-  
440 ample from eastern turkey, *Geophys. Res. Lett.*, 30, 2003.
- 441 Schulte-Pelkum, V., P. S. Earle, and F. L. Vernon, Strong directivity of ocean-  
442 generated seismic noise, *Geochemistry, Geophysics, Geosystems*, 5, 3004–+, doi:  
443 10.1029/2003GC000520, 2004.
- 444 Sens-Schönfelder, C., and U. Wegler, Passive image interferometry and seasonal variations  
445 of seismic velocities at Merapi Volcano, Indonesia, *Geophysical Research Letters*, 33,  
446 21,302–+, doi:10.1029/2006GL027797, 2006.
- 447 Seriff, A. J., C. J. Velzeboer, and R. J. Haase, Possible P-Wave Observations in Short-  
448 Period Seismic Noise, *Geophysics*, 30, 1187–+, doi:10.1190/1.1439709, 1965.

- 449 Shapiro, N. M., and M. Campillo, Emergence of broadband Rayleigh waves from cor-  
450 relations of the ambient seismic noise, *Geophysical Research Letters*, *31*, 7614–+, doi:  
451 10.1029/2004GL019491, 2004.
- 452 Shapiro, N. M., M. Campillo, L. Stehly, and M. H. Ritzwoller, High-Resolution  
453 Surface-Wave Tomography from Ambient Seismic Noise, *Science*, *307*, 1615–1618, doi:  
454 10.1126/science.1108339, 2005.
- 455 Snieder, R., Extracting the Green’s function from the correlation of coda waves: A  
456 derivation based on stationary phase, *Physical Review E*, *69*(4), 046,610–+, doi:  
457 10.1103/PhysRevE.69.046610, 2004.
- 458 Stehly, L., M. Campillo, and N. M. Shapiro, A study of the seismic noise from its long-  
459 range correlation properties, *Journal of Geophysical Research (Solid Earth)*, *111*(B10),  
460 10,306–+, doi:10.1029/2005JB004237, 2006.
- 461 Stehly, L., B. Fry, M. Campillo, N. M. Shapiro, J. Guilbert, L. Boschi, and D. Giardini,  
462 Cross-correlation of random fields: mathematical approach and applications, *Geophys-*  
463 *ical Journal International*, in press, 2009.
- 464 Tanimoto, T., S. Ishimaru, and C. Alvizuri, Seasonality in particle motion of  
465 microseisms, *Geophysical Journal International*, *166*, 253–266, doi:10.1111/j.1365-  
466 246X.2006.02931.x, 2006.
- 467 Toksöz, M. N., and R. T. Lacoss, Microseisms: Mode Structure and Sources, *Science*,  
468 *159*, 872–873, 1968.
- 469 Yang, Y., and M. H. Ritzwoller, Characteristics of ambient seismic noise as a source  
470 for surface wave tomography, *Geochemistry, Geophysics, Geosystems*, *9*, 2008–+, doi:  
471 10.1029/2007GC001814, 2008.

472 Yang, Y., M. H. Ritzwoller, A. L. Levshin, and N. M. Shapiro, Ambient noise Rayleigh  
473 wave tomography across Europe, *Geophysical Journal International*, 168, 259–274, doi:  
474 10.1111/j.1365-246X.2006.03203.x, 2007.

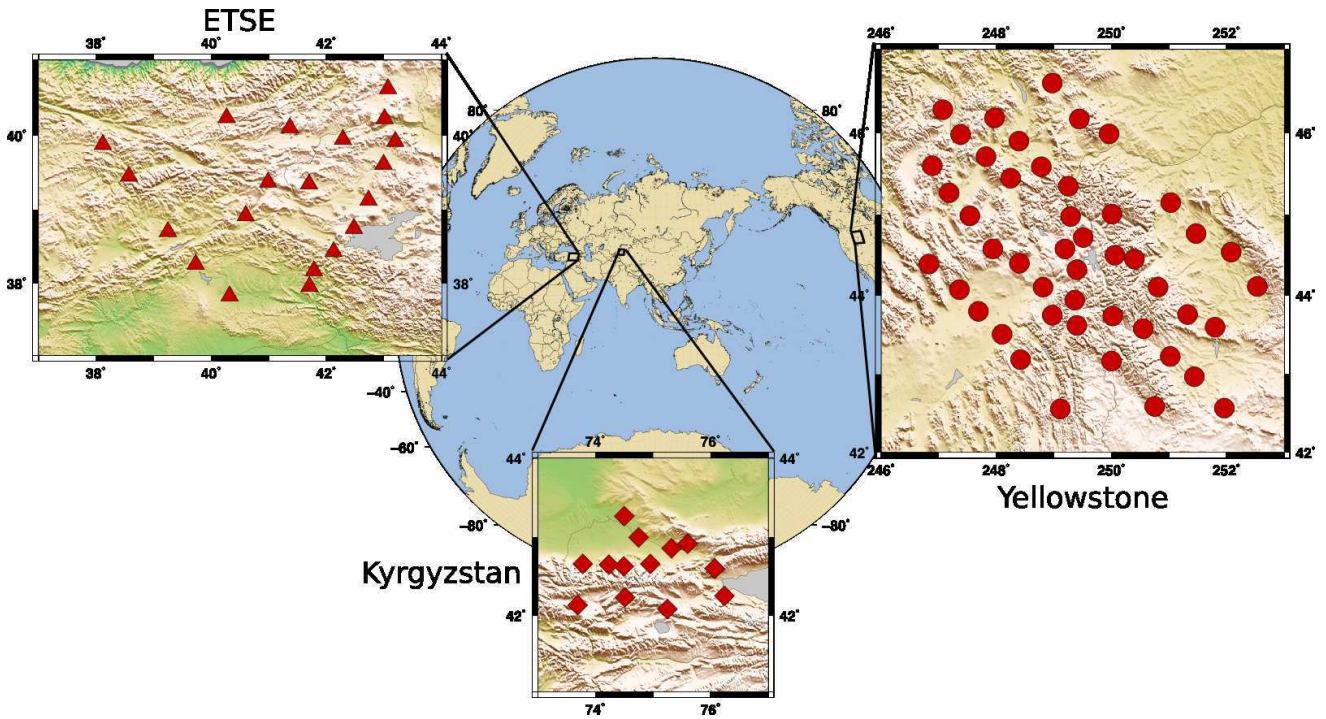
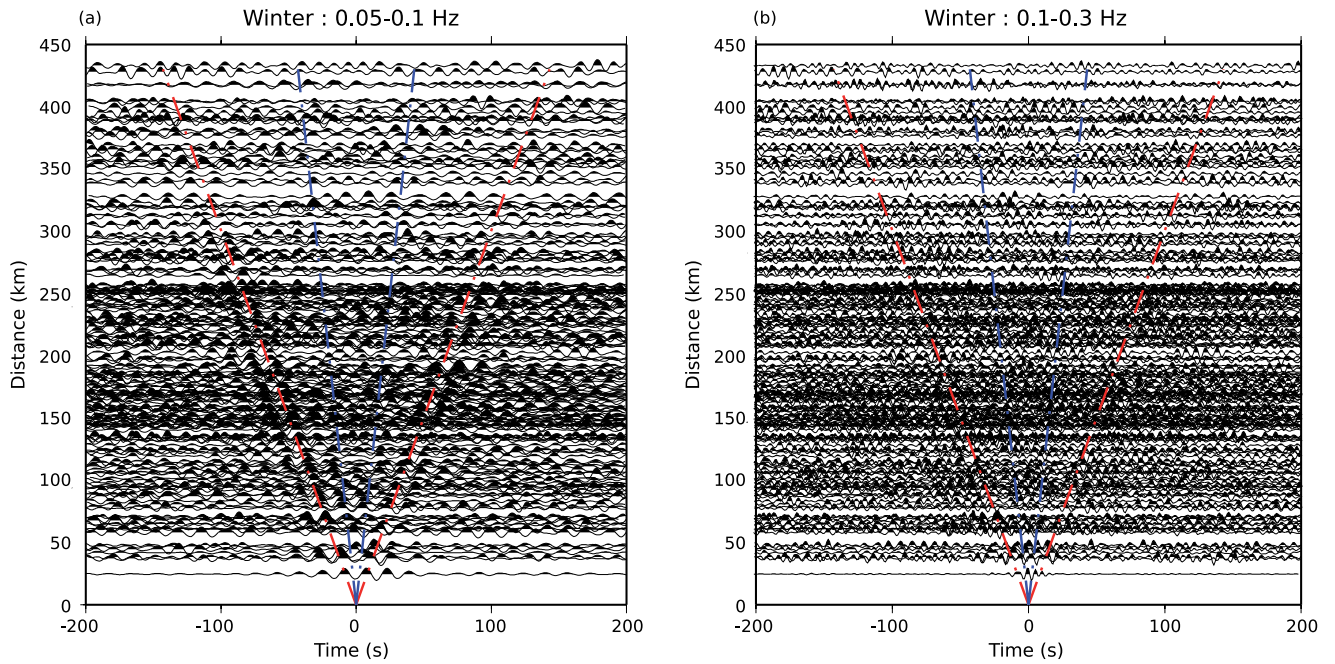
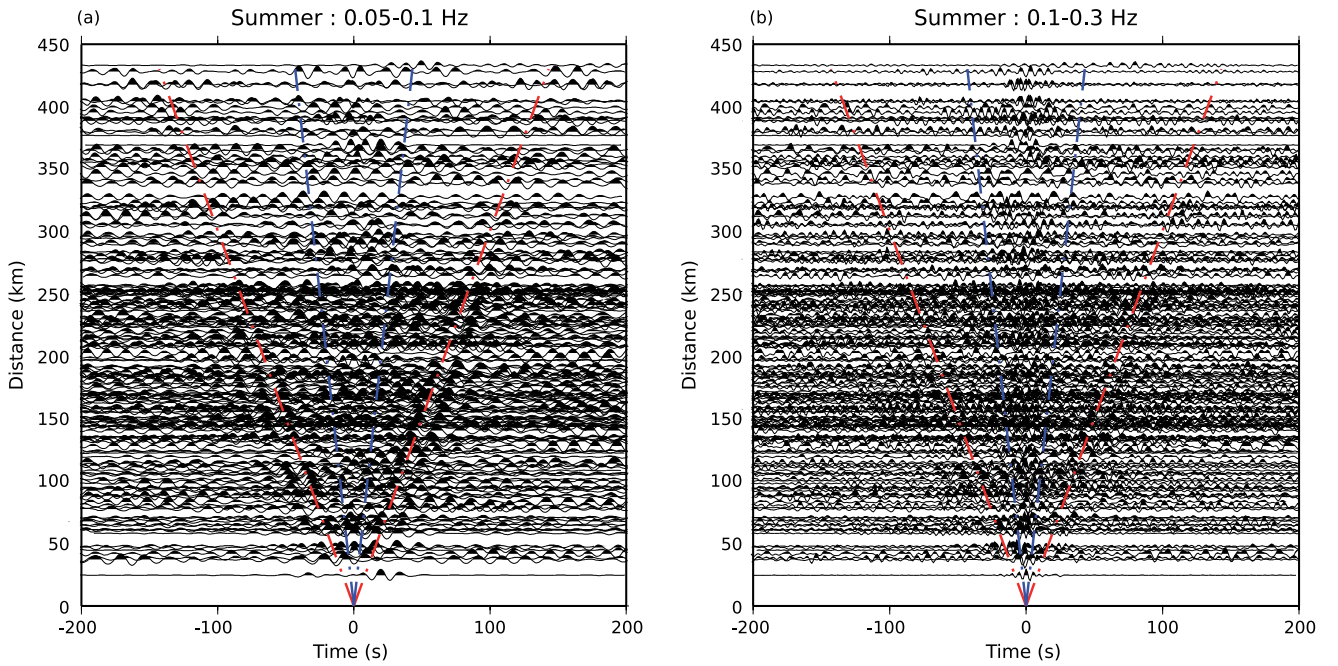


Figure 1. Maps of ETSE, Yellowstone and Kyrgyzstan networks





**Figure 2.** Cross-correlations of vertical component records between stations of the ETSE network stacked for months between September and March (winter) for years 1999, 2000 and 2001 plotted as function of the distance between the pair of stations in the 0.05-0.1 Hz (a) and 0.1-0.3 Hz (b) frequency band.



**Figure 3.** Cross-correlations of vertical component records between stations of the ETSE network stacked for months between April and August (summer) for years 1999, 2000 and 2001 plotted as function of the distance between the pair of stations in the 0.05-0.1 Hz (a) and 0.1-0.3 Hz (b) frequency band.

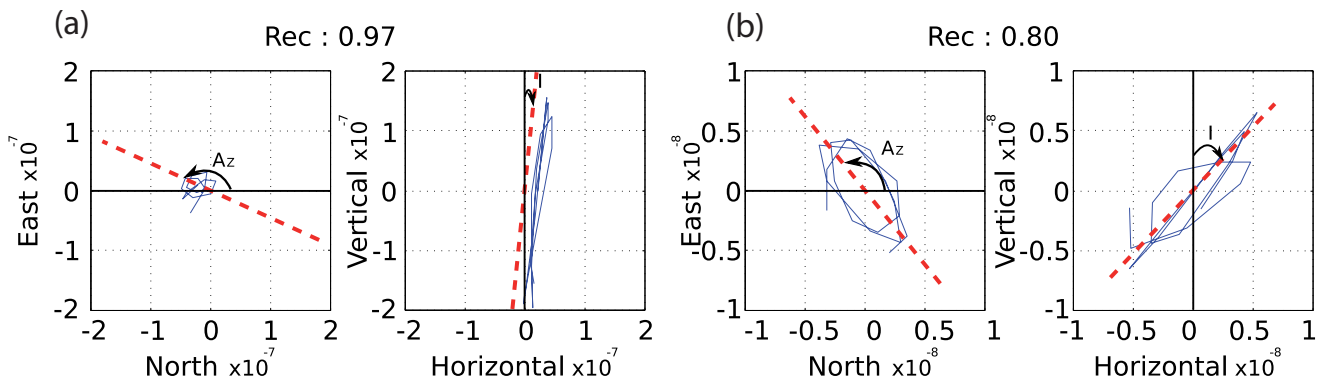


**Figure 4.** Particle motion for 2 station pairs from noise correlations in the  $[-10s; +10s]$  time window for the band 0.1-0.2 Hz. (a) : cross-correlations between KARS and KOTK (distance 391 km) for the 10/30/1999 ; (b) : cross-correlations between KARS and ILIC (distance 404 km) for the 03/23/2000. *Rec* is the rectilinearity coefficient defined by Eq . 1. Red dashed lines show the incidence angle and the azimuth measured from the covariance method.

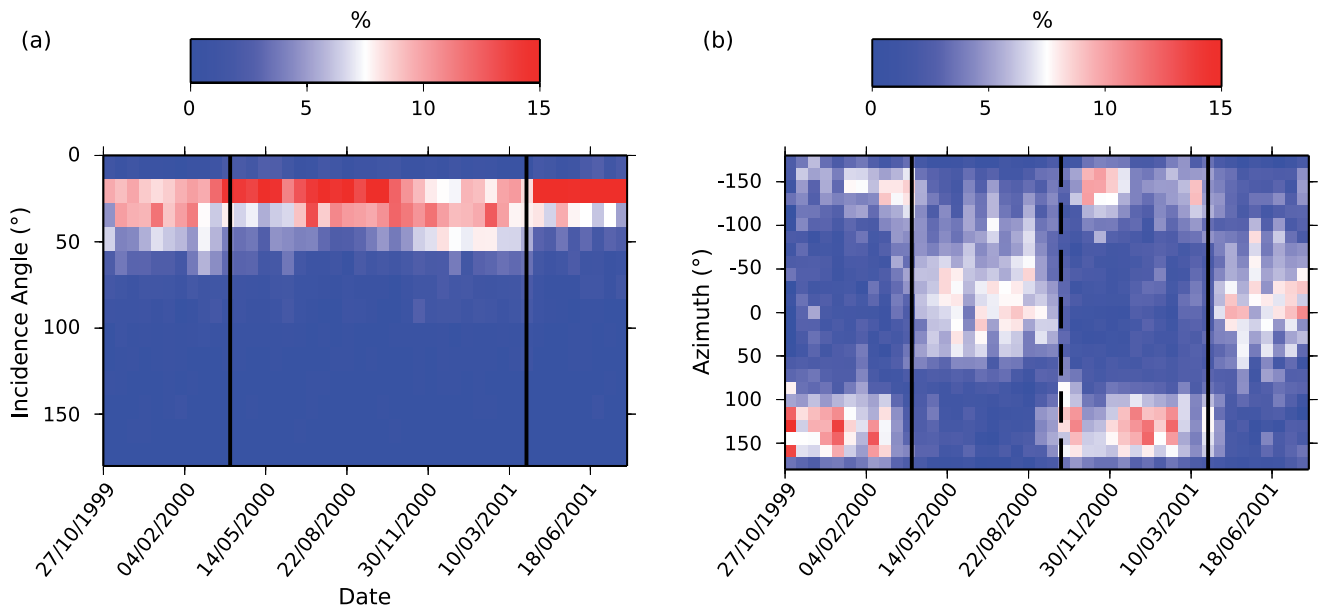


**Figure 5.** Probability of occurrence of a given value of the incidence angle (a) and of the azimuth (b) for 20 days time periods for all station pairs of the ETSE network. Continuous black lines correspond to 04/01/2000 and 04/01/2001 and black dashed lines to 10/01/2000

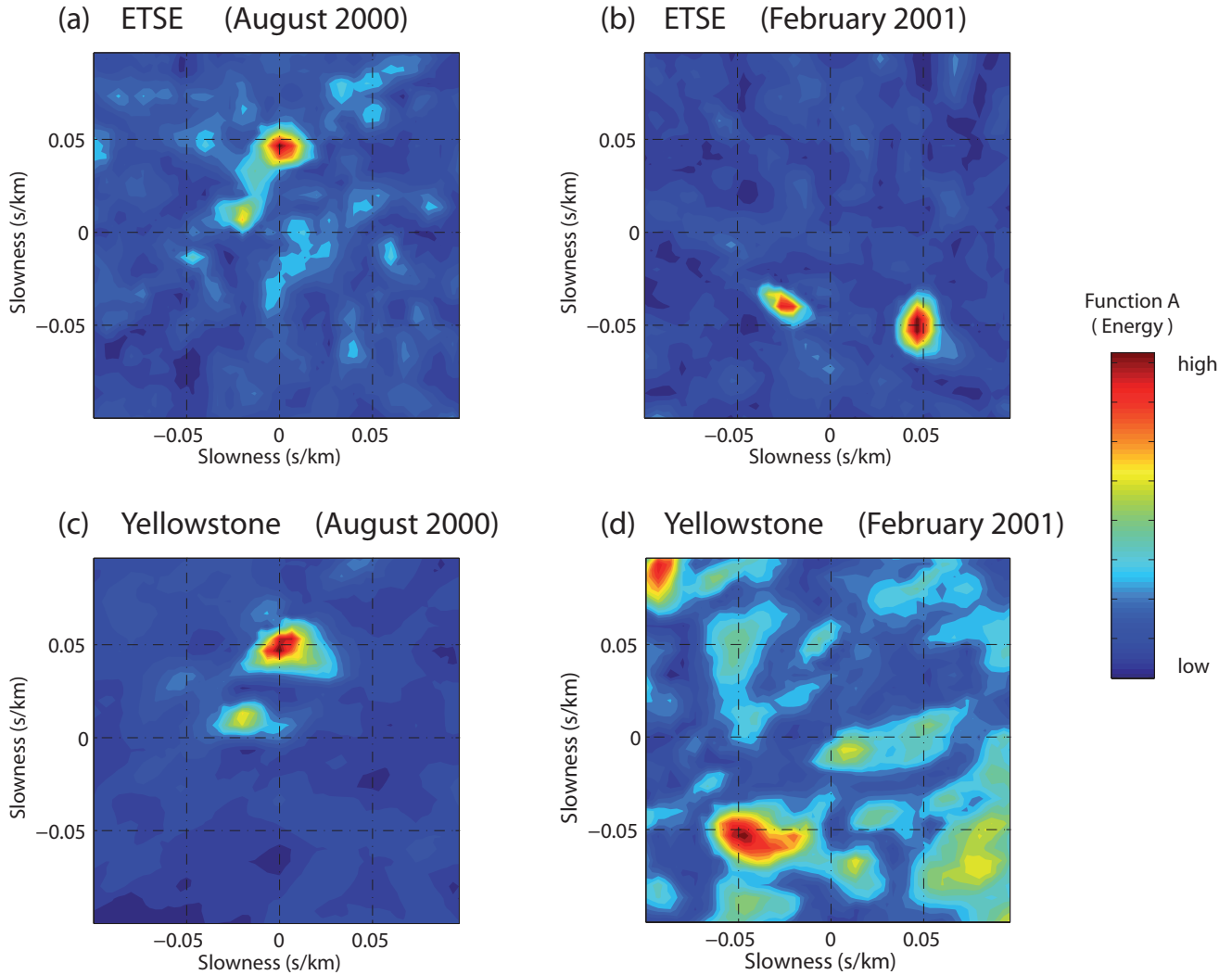


**Figure 6.** Beamforming result of the Yellowstone and ETSE networks for August 2000 and February 2001 around the secondary microseismic peak (0.1-0.3 Hz). Axes are in s/km.

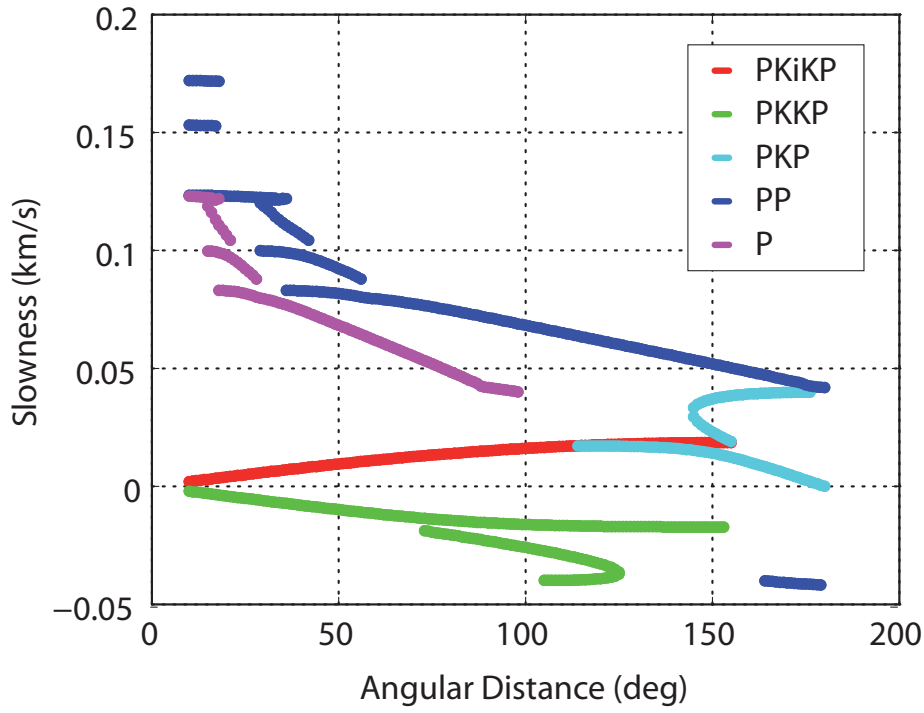


**Figure 7.** Variations of slowness (s/km) with respect to the angular distance (deg) for P, PP, PKP, PKiKP and PKIKP phases.

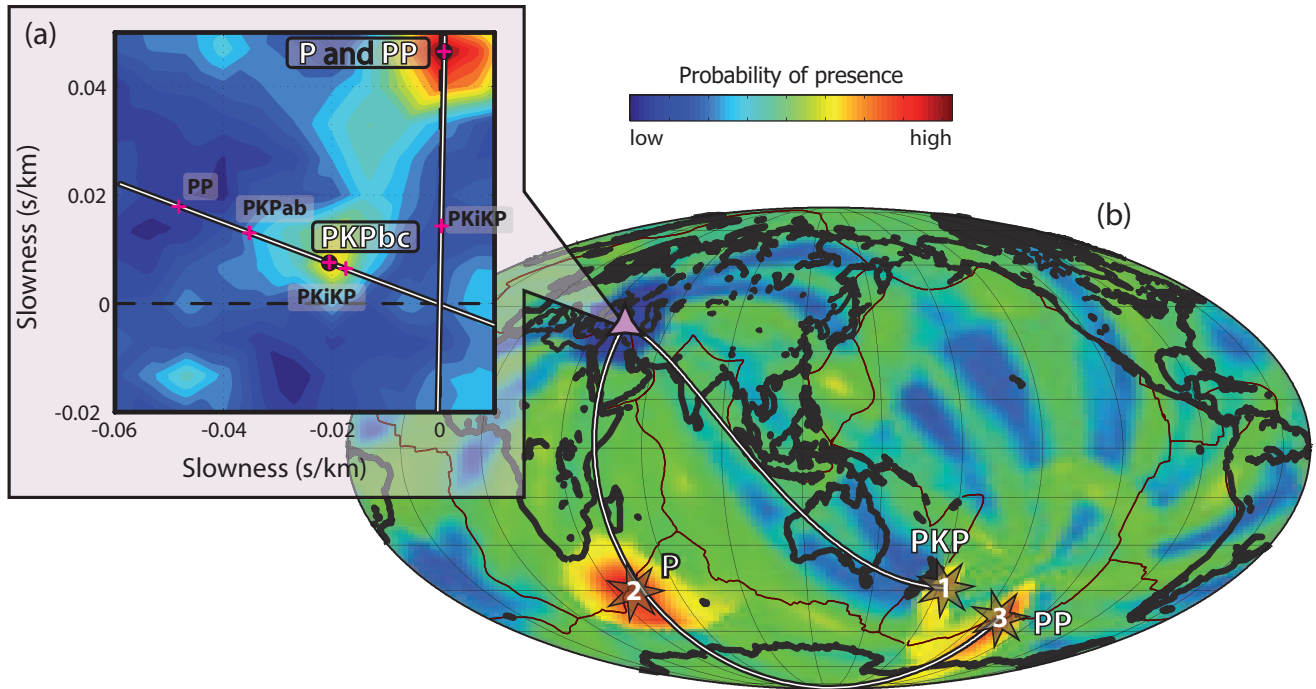


**Figure 8.** Illustration of projection of the beamforming results on the Earth's surface (see text for explanations). (a) Results of the beamforming analysis of noise cross-correlations computed during August 2000 for the 0.1-0.3 Hz frequency band between stations of the Turkey network plotted as function of horizontal slowness. (b) Projection of these results on the Earth surface.

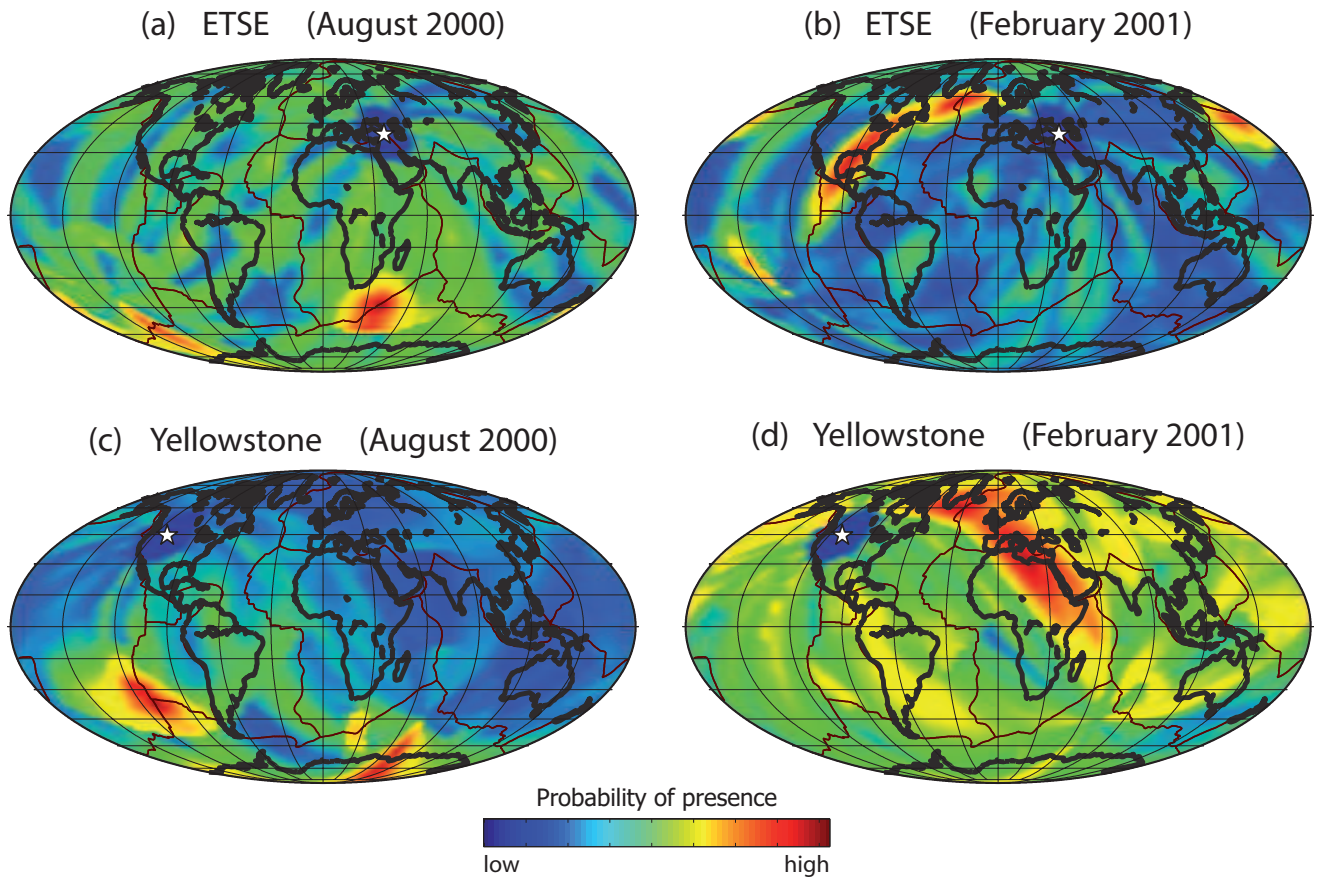


**Figure 9.** Projection results of the Yellowstone and ETSE networks for August 2000 and February 2001 around the secondary microseismic peak (0.1-0.3 Hz).

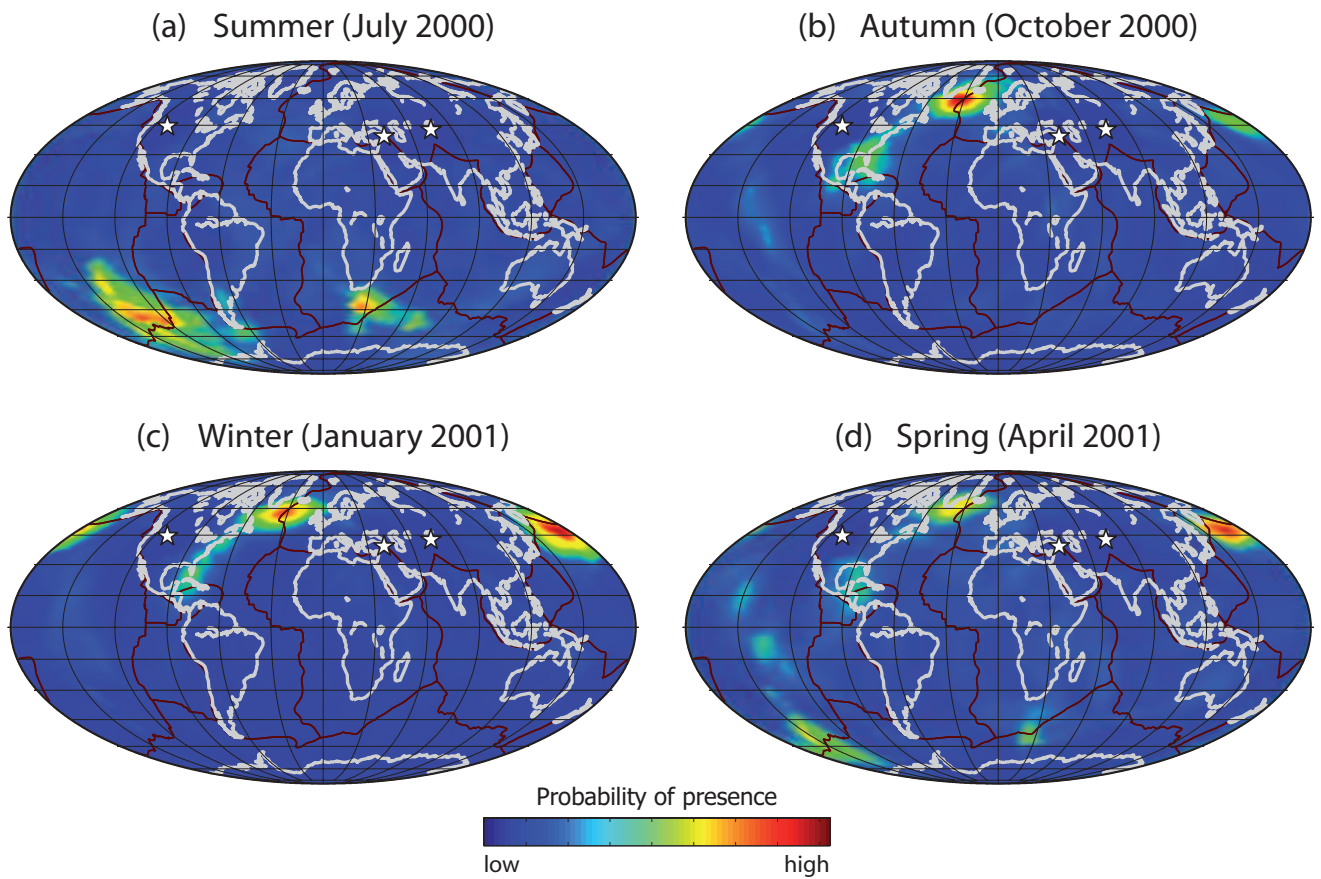


**Figure 10.** Seasonal variation of the location of P-wave seismic noise sources in the secondary microseismic band (0.1-0.3 Hz).



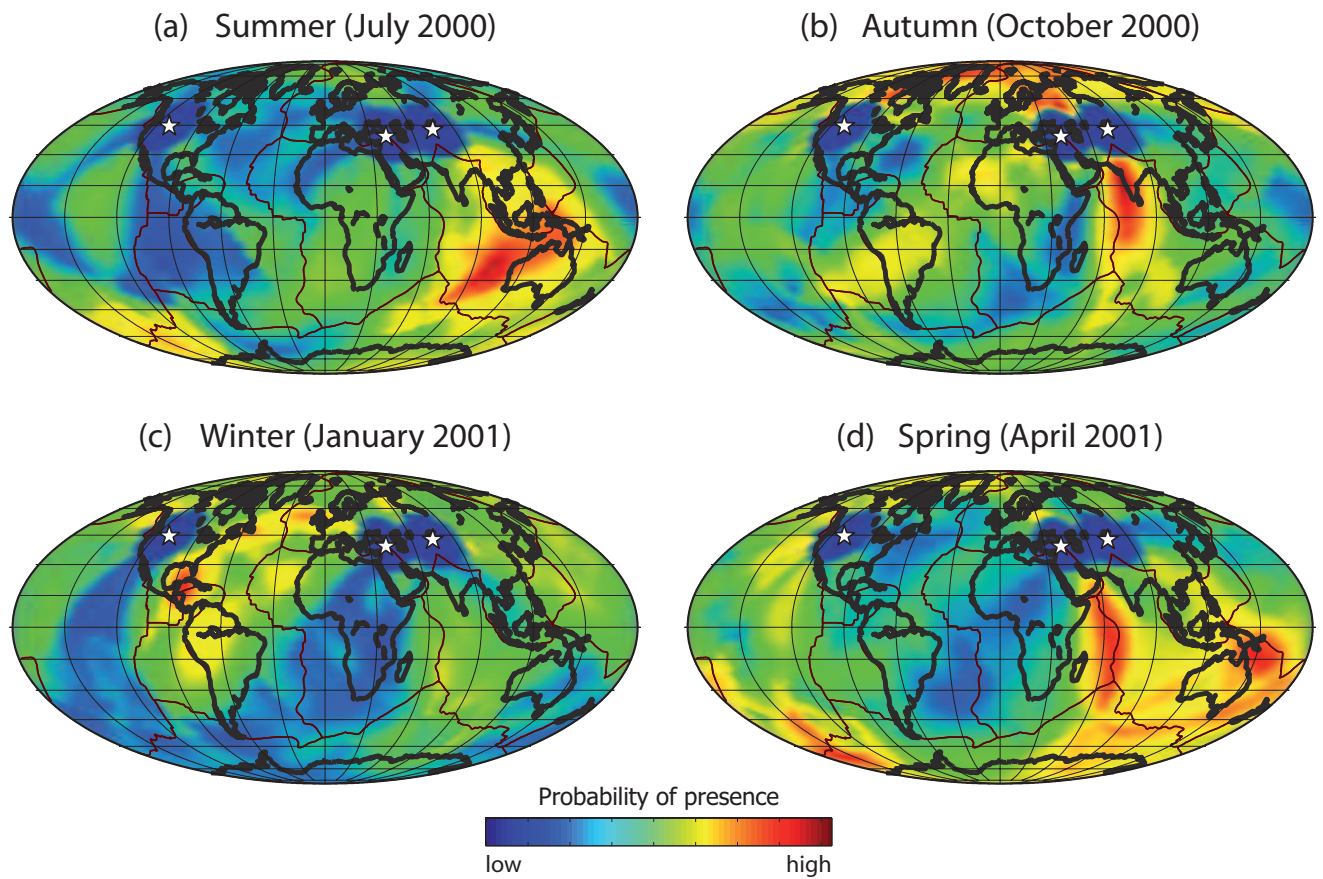


**Figure 11.** Seasonal variation of the localization of seismic noise in the primary microseismic bands (0.05-0.1 Hz).

## Appendix A: Wave polarization analysis from cross-correlations

475 We consider a plane wave with amplitude  $A$ , wave vector  $\vec{k}$  and pulse shape  $v(t)$ . The azimuth  
 476 ( $Az$ ) is defined as the angle between the North and the projection of the wave vector in the  
 477 horizontal plane. In the vertical plane, the incidence angle ( $I$ ) is the angle between the vertical  
 478 and the wave vector. Equation A1 gives the general form of a 3-component record of the signal  
 479 that will be used for this demonstration :

$$\begin{aligned}
 S_N(t) &= A \sin(I) \cos(Az) v(t - T), \\
 S_E(t) &= A \sin(I) \sin(Az) v(t - T), \\
 S_Z(t) &= A \cos(I) v(t - T),
 \end{aligned}
 \tag{A1}$$

480 where  $T$  is the arrival time of the signal at the station.

481 This plane wave is recorded at two different stations A and B at times  $T = t_A$  and  $T = t_B$ .  
 482 We compute three cross-correlations between the vertical component of station A and the 3  
 483 components of station B. They are :

$$\begin{aligned}
 ZN(t) &= A^2 \cos(I) \sin(I) \cos(Az) V(t), \\
 ZE(t) &= A^2 \cos(I) \sin(I) \sin(Az) V(t), \\
 ZZ(t) &= A^2 \cos^2(I) V(t),
 \end{aligned}
 \tag{A2}$$

where :

$$V(t) = \int_{-\infty}^{+\infty} v(\tau) \bar{v}[\tau - (t_B - t_A) - t] d\tau
 \tag{A3}$$

484 is the time correlation function and  $\bar{v}(t)$  the complex conjugate of  $v(t)$ .

485 The definition of the covariance between two signals ( $E$  and  $F$ ) in the time window  $[T_1, T_2]$  is  
 486 given by :

$$Cov_{EF} = \int_{T_1}^{T_2} E(t)F(t)dt. \quad (A4)$$

487 For North and East component records of station  $A$ , we select a time window including the  
 488 signal ( $t_A \in [T_1, T_2]$ ) and we compute the covariance defined by equation A4 to obtain :

$$Cov_{NE} = \int_{T_1}^{T_2} A^2 \sin^2(I) \cos(Az) \sin(Az) v(t - t_A) v(t - t_A) dt,$$

$$Cov_{NE} = A^2 \sin^2(I) \cos(Az) \sin(Az) C, \quad (A5)$$

489 where  $C = \int_{T_1}^{T_2} v(t - t_A) v(t - t_A) dt$  is a non-null constant.

490 We apply the same computation to all pairs of records at station  $A$  and we obtain the covariance  
 491 matrix of the 3-component record :

$$S_{CovS_A} = C \cdot M, \quad (A6)$$

where :

$$M = \begin{pmatrix} \cos^2(I) & \cos(I) \sin(I) \cos(Az) & \cos(I) \sin(I) \sin(Az) \\ \cos(I) \sin(I) \cos(Az) & \sin^2(I) \cos^2(Az) & \sin^2(I) \cos(Az) \sin(Az) \\ \cos(I) \sin(I) \sin(Az) & \sin^2(I) \cos(Az) \sin(Az) & \sin^2(I) \sin^2(Az) \end{pmatrix}. \quad (A7)$$

492 We consider the definition of the covariance (Equation A4) and the definition of the cross-  
 493 correlations between 2 stations (Equation A2) to compute the covariance between ZE and ZN  
 494 cross-correlations. We select a time window  $[T_1; T_2]$  of the correlation which includes the corre-  
 495 lation of the initial signal :

$$\begin{aligned}
Cov_{Z_A E_B - Z_A N_B} &= \int_{T_1}^{T_2} A^4 \cos^2(I) \sin^2(I) \cos(Az) \sin(Az) V(t) V(t) dt, \\
Cov_{Z_A E_B - Z_A N_B} &= A^4 \cos^2(I) \sin^2(I) \cos(Az) \sin(Az) C_{Corr},
\end{aligned} \tag{A8}$$

496 where  $C_{Corr} = \int_{T_1}^{T_2} V(t) V(t) dt$  is a non-null constant.

497 The covariance matrix for cross-correlations is computed from Equations A2 and A4 :

$$S_{CovCorr_{A,B}} = A^4 \cos^2(I) C_{Corr} \cdot M. \tag{A9}$$

$$S_{CovCorr} = A^2 \cos^2(I) \frac{C_{Corr}}{C} S_{CovS_A}. \tag{A10}$$

498 where  $A^2 \cos^2(I) \frac{C_{Corr}}{C}$  is a non-null constant. From Equation A10 we conclude that, in the  
499 case of a plane P-wave, the covariance matrix for the 3-component record at a single station  
500 and the covariance matrix for the cross-correlations between 2 stations ( $S_{CovS_A}$  and  $S_{CovCorr_{A,B}}$ ,  
501 respectively) differ only by a scalar factor. Therefore, the eigenvectors of those matrix are the  
502 same which prove the polarization analysis can be performed either on cross-correlation or on 3  
503 component records.